Published in Physical Review B 70, issue 165114, 1-10, 2004
which should be used for any reference to this work

Fermi-surface topology of rare-earth dihydrides

C. Koitzsch,[1,*] J. Hayoz,[2,†] M. Bovet,[1] F. Clerc,[1] L. Despont,[1] C. Ambrosch-Draxl,[3] and P. Aebi[1]
[1]*Institut de Physique, Université de Neuchâtel, Rue A.-L. Breguet 1, CH-2000 Neuchâtel, Switzerland*
[2]*Institut de Physique, Université de Fribourg, Pérolles, CH-1700 Fribourg, Switzerland*
[3]*Institute of Theoretical Physics, Karl-Franzens-University Graz, Universitätsplatz 5, A-8010 Graz, Austria*

We report high-resolution angle-resolved photoemission experiments on epitaxial thin films of different rare-earth (RE) dihydrides (RE=Gd,La) and of YH_2 and ScH_2. It is found through *ab initio* calculations and confirmed by Fermi surface mapping that the electronic structure becomes very similar upon hydrogenation, rendering the studied dihydrides isoelectronic. We propose that the dihydride phase acts as a common precursor state for the formation of the insulating trihydride phase. For states with higher binding energies (which exhibit considerable H character) the agreement between calculation and measurement is less convincing. Independent of the difficulties to describe these hydrogen related states, we note in the comparison between experiment and calculation a very convincing description of the Fermi surface for the dihydrides. Therefore we trace the apparent inability of density, functional theory to describe the hygrogenation up to the trihydride phase to an insufficient description of hydrogen states in general and, in particular, involving octahedral sites.

I. INTRODUCTION

The valence electronic structure of rare-earth hydrides is both fundamentally interesting and technologically important. Fundamentally interesting, because one finds interesting phenomena, e.g., electronic and magnetic ordering and metal-insulator (Me-I) transitions for a whole class of materials,[1] hence allowing the possibility to study these effects for different hydrogen concentrations and various metallic host lattices. Initiated by potential applications, the phase transition between the dihydride and trihydride phase received recently tremendous interest, since the structural transition between the fcc dihydride and the hcp trihydride (exception is LaH_{2+x} which remains cubic) is accompanied by a spectacular change in the optical properties. The so-called "switchable mirror" transition for the reversible phase change from a metallic reflecting dihydride to a transparent insulating trihydride was first described by Huiberts *et al.*[2] for YH_x and LaH_x. The search for other reliable and fast switching materials beside the original systems revealed an astonishing diversity of materials for which a hydrogen induced Me-I transition occurs, basically comprising the whole rare earths, but also lighter materials such as Mg (Ref. 3) and different ternary compounds. The apparent universal nature of the Me-I transition upon hydrogenation is one of the motivations to investigate in this work the electronic structure of the metallic dihydride, which can be perceived as a *precursor phase*. We report on high-resolution angle-resolved photoemission (ARPES) experiments on epitaxial thin films of different rare-earth dihydrides (GdH_2, LaH_2) and of YH_2 and ScH_2. In the following, for argumentative simplicity, Y and Sc are referred to as rare earths (RE) as well.

The aforementioned insulating trihydride phase posed a very demanding challenge for modern electronic structure calculations. *Ab initio* calculations with the local-density approximation (LDA) were unable to reproduce the insulating ground state at all. Only a structural deviation[4,5] led to a small gap via a symmetry lowering. The discrepancy in gap size between calculation and the experiment[6,7] is comparable to known strongly correlated systems and different models were proposed, which ascribed the Me-I transition to strong electron correlations on H sites.[8,9] Recently GW calculations were able to reproduce the experimental gap and it was claimed, that the insulating trihydride is similar to a conventional semiconductor.[10–12] From a practical point of view it seems that the GW calculations only lead to a shift of LDA bands with no significant modifications in terms of bandwidth or band topology. It is at present still unclear, where the limitations of LDA are and if there is a general recipe how to correct LDA results. It is therefore very interesting to test LDA for the dihydride phase, which is still metallic (therefore presumably accessible with LDA) but can be viewed in a simplified view as a hydrogen deficient trihydride. We therefore utilized an *ab initio* augmented plane wave plus local orbital (APW+lo) code[13] with the generalized gradient approximation (GGA) (Ref. 14) to calculate the electronic structure and compare it to the experimental ARPES results.

The paper is organized as follows. The following section deals briefly with the experimental setup and the sample preparation. Furthermore the employed APW+lo *ab initio* electronic structure calculations are described. The main Sec. III gives an introduction into the electronic structure of rare-earth dihydrides based on band-structure calculations. Already existing models are briefly discussed in this context. Furthermore we present the angle-resolved photoemission data for the different rare-earth hydrides and focus on YH_2 for an indepth comparison to computationally obtained results. In Sec. IV we discuss our findings in a more general context and comment on the recent debates about the Me-I transitions and various structural and magnetic ordering phenomena in this class of materials. The paper finishes with conclusions in Sec. V.

II. EXPERIMENT AND CALCULATION

The preparation of contamination-free single crystalline dihydride films imposes stringent requirements in terms of base pressure during evaporation of the pure metals and hydrogen gas purity due to the strong affinity to oxygen and the subsequent undesired formation of surface or even bulk oxide. Therefore we took the utmost care in outgassing the water-cooled *e*-beam evaporator ensuring that evaporation was achieved below 4×10^{-10} mbar. Metal (200 Å) was evaporated in a hydrogen pressure of 4×10^{-6} mbar on a clean *W*(110) single crystal held at 500 K. The utilized hydrogen was filtered through a Pd-Ag permeation tube.[15] The resulting films are single crystalline. Low-energy electron diffraction (LEED) shows no superlattice spots, just a 1×1 surface unit cell with lattice parameters equal to the bulk values within the experimental error of ±0.3 Å. The film thickness of 200 Å is sufficient to exclude any quantum size effects[16,17] and should allow for a sufficient strain release.

The photoemission experiments were performed immediately after film growth, *in situ* in a modified VG ESCALAB Mk II spectrometer with a base pressure lower than 10^{-10} mbar. Surface cleanliness was ensured by the absence of O 1*s* and C 1*s* core level emission in the x-ray photoelectron spectrum employing Mg K_α radiation. The angular dependence of emission from metal core levels over the full hemisphere was measured via rotating the sample with a two-axis sample goniometer enabling sequential computer-controlled sample rotation.[18,19] This measurement mode is commonly called x-ray photoelectron-diffraction (XPD), for a review see e.g., Ref. 20. All prepared films were found to exhibit fcc stacking with two domains, both oriented in (111) direction but rotated 180° with respect to each other. The fcc crystal structure immediately confirms the preparation of the dihydride phase. We could not detect traces of hcp stacking, which translates the hydrogen content close to a stoichiometric dihydride. Nevertheless, a partial occupation of octahedral sites and/or the existence of tetrahedral vacancies cannot be ruled out completely. Details of the structural analysis via x-ray photoelectron-spectroscopy and -diffraction are not presented here, the interested reader is referred to Ref. 21. The ARPES measurements were performed via sequential angle-scanning data acquisition. The accuracy and efficiency of this method was demonstrated for two-[22] and three-dimensional[23] materials. The obvious advantage of this method is the uniform sampling density over a wide range of *k*-space and hence a global view of direct transitions crossing E_F. The experimental procedure was outlined in Ref. 23 and the reader is referred to this work for details. We furthermore present conventional $E(k)$ scans, which are restricted to the $[\bar{\Gamma}\,\bar{M}]$ high symmetry direction covering an energy window of 7.48 eV. These measurement modi are complementary in terms of range in *k*-space and energy and provide a global and yet detailed view of the electronic structure in the vicinity of the Fermi level. All presented measurements were obtained using monochromatized He I radiation,[24] the combined angular resolution of sample manipulator and energy analyzer is ≈1° and the energy resolution 50 meV. All calculations rely on the published structural data from

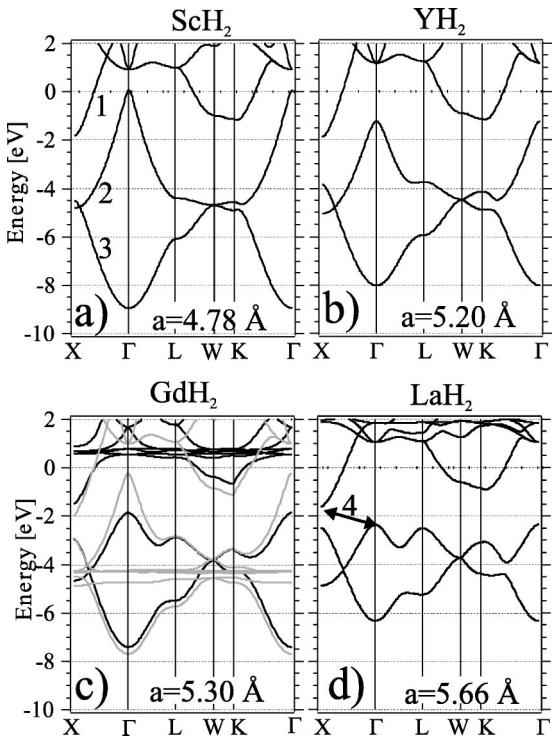

FIG. 1. Band structure along high-symmetry directions for (a) ScH_2, (b) YH_2, (c) GdH_2, and (d) LaH_2; one notices three bands labeled 1,2, and 3 with an indirect gap, respectively, overlap between band 1 and band 2 marked as feature 4 in (d). The calculation for GdH_2 is spin polarized in order to avoid a placement of the 4*f* levels at the Fermi level, the majority bands are shown in gray.

Pearsson.[25] The electronic structure calculations are based on density-functional theory (DFT) and the APW+lo code Wien2k (Ref. 13) was employed. There the unit cell is divided into nonoverlapping atomic spheres (muffin tin) and an interstitial region.[26] In the muffin tin region the basis functions are comprised of atomiclike wave functions while the interstitial region is described with plane-wave basis functions. A muffin tin radius for rare-earth atoms and hydrogen atoms of 1.16 Å and 0.85 Å was assumed, respectively. Self consistency was judged, when the total energy change was less than 0.1 mRy in subsequent cycles. The calculation was based on 10 000 *k* points, which corresponds to 286 *k* points in the irreducible wedge of the Brillouin zone (BZ).

III. EXPERIMENTAL AND THEORETICAL RESULTS

A. General electronic properties of (Sc,Y,Gd,La)—dihydrides

The electronic structure of RE dihydrides and their related compounds YH_2, ScH_2 was already investigated more than 20 years ago by photoemission.[27–29] These studies employed polycrystalline samples and hence only the effects of hydrogenation on the density of states were investigated. These experiments were combined with theoretical calculations.[30–33] In order to allow for a comparison of our LDA results with already published calculations, we show in Fig. 1 conventional band-structure plots based upon converged calculations for the studied compounds. A very good

agreement to the aforementioned older calculations is achieved. This points to an apparent robustness of the band topology in terms of technique and self consistency, since older calculations are often not self consistent and/or use different basis sets. Nevertheless small shifts in the relative positions of bands are possible.

The band structures, presented in Fig. 1 are very similar. One notices three bands below the Fermi level, marked with 1,2, and 3 for the case of ScH_2 in Fig. 1(a). The pioneering calculation of Swietendick[30,31] already attributed *d*-like metallic character to band one, hydrogen antibonding character to band two, and mixed metal-hydrogen (Me-H) character to band three. The nature of bonding in these compounds must be discussed in terms of interaction between metal *d* states and hydrogen 1*s* states. Metal sites are surrounded by eight hydrogen atoms situated on tetrahedral sites in the fcc lattice. The atomic environment of the metal sites is comprised of a cube with hydrogen atoms at the cube corners and the metal atom at the center. An equal occupation of the three t_{2g} orbitals, which is required by the cubic symmetry, leads to charge maxima along the cube diagonals, the [111]-direction. By the same argument one can correlate the remaining two e_g orbitals with bonding orbitals to octahedral sites, which are unoccupied in the dihydride phase.[33] The formation of a Me-H bonding band with a binding energy at Γ between −6 and −9 eV poses the question of ionicity of this bond. Charge-transfer analysis[33] points to an effective charge transfer away from the metal site to the tetrahedral hydrogen sites.

If one compares the band structure of the different dihydrides, one notices subtle differences. The bandwidth of hydrogen related bands (band two and three in Fig. 1) increases with decreasing lattice constant. While there is an indirect gap of 0.73 eV between band two at Γ and band 1 at *X* for the alloy with the largest lattice constant LaH_2, marked as feature 4, there is considerable overlap of 0.65 eV for YH_2 and 1.89 eV for ScH_2 between band one and band two. It is interesting to note that the position of band one with respect to the Fermi level does not significantly change for the different alloys. In contrast, the maximum of the hydrogen antibonding band at Γ moves away from the Fermi level to larger binding energies for increasing lattice constants. This shift leads finally to the aforementioned indirect gap of 0.73 eV between band 1 and band 2 for LaH_2. Band 3 exhibits an opposite trend, here the band minimum at Γ shifts upwards from a binding energy of −8.9 eV for ScH_2 to −6.3 eV for LaH_2. The observed increase of bandwidth with decreasing lattice constant supports the proposed assignment of antibonding and respectively bonding character to band 2 and band 3. The increased bandwidth for small lattice constants can then be understood as an increased level spacing for decreasing separations.

In order to confirm this presumed lattice constant scaling, band-structure calculations for ScH_2 with different lattice constants were performed. The results (not shown) confirm this assumption. It seems that the band structure for hydrogen related states can be tuned quite freely by changing the lattice constant, but the metal derived *d* band remains rather unaffected. Based on these band structures one expects very similar Fermi surface topologies for the different dihydrides since band one is solely responsible for the Fermi surface, with the exception of ScH_2, where the calculation yields a small pocket at Γ derived from the hydrogen related band 2. We are not concentrating on the implications of this small pocket on the electronic structure of ScH_2 since our measurement geometry is not sensitive to *k* points exactly at Γ, as it will be shown later in Sec. III B and as it would be necessary to confirm this point. In the following we concentrate on band 1. There one sees a Fermi level crossing between Γ and *X* and between Γ and *K* and between *L* and *W*. One does not observe a Fermi level crossing between Γ and *L*. This points to a connected Fermi surface, where the necks extend along the ΓL direction, hence one does not observe a crossing in this direction. This will be discussed in more detail in conjunction with the experimentally obtained Fermi surface maps.

B. Experimental data and calculation

The following discussion of the electronic structure takes mainly place in reciprocal space, in the surface Brillouin zone (SBZ). Figure 2(a) shows the SBZ for a fcc (111) orientated surface, the scale is adapted to YH_2. The various high-symmetry points originate from a projection of the three-dimensional (3D) bulk BZ onto the surface. For the specific $\bar{\Gamma}\,\bar{M}$ direction, the ΓKLUX plane is projected onto the surface, as it is shown in Fig. 2(b). It becomes obvious, that the *a priori* inequivalent $\bar{M}$ and $\bar{M}'$ points stem from a projection of the *X*, respectively, *L* point of the bulk BZ. This inequivalency is lifted for our measurement geometry, because the photoemission signal is integrated over two film domains. The second film domain is rotated 180° with respect to the first. The bulk BZ of this second domain is shown in gray and is constructed via a rotation around the (111) axis. As a result of this rotation the $\bar{M}$ and $\bar{M}'$ points become indistinguishable. A photoemission experiment allows for an exact determination of the band dispersion $E(k_\parallel)$ in the SBZ, due to the conservation of the parallel wave-vector component, $k_\parallel$, in the photoemission process. The perpendicular wave-vector component, $k_\perp$, is less well defined and its reconstruction is based on the free-electron final state (FEFS) assumption. Here one assumes for the photoemission final state a free-electron parabola. This assumption appears adequate for the reconstruction of the perpendicular wave vector component for excitations in the employed energy range.[23] Within this approximation, energy and momentum conservation correspond to spherical cuts through the three dimensional BZ. The radius of the cut k_0 is determined via Eq. (1) by the photon energy ($\hbar\omega$=21.2 eV), the inner potential V_0, the work function ϕ and the probed initial state energy E_B.

$$k_0 = 0.51\sqrt{\hbar\omega - |E_B| - |\phi| + |V_0|}, \tag{1}$$

$$k_\parallel(\theta) = 0.51\sqrt{\hbar\omega - |E_B| - |\phi|}\,\sin[\theta]. \tag{2}$$

k_0 and $k_\parallel$ are the length of the FEFS wave vector in the solid and the conserved parallel wave-vector component, respectively. Equations (1) and (2) are such that energies are in [eV] and wave vectors in [$Å^{-1}$].

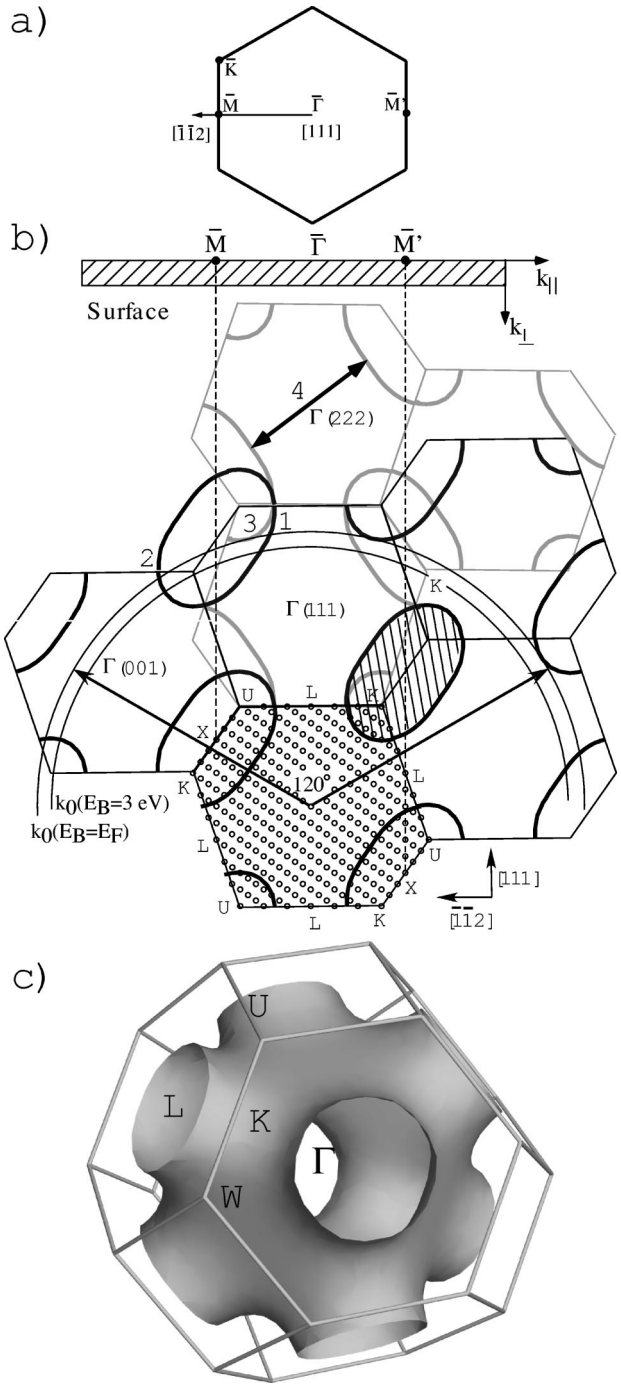

FIG. 2. (a) Surface Brillouin zone for YH_2. (b) Side view of the BZ for a fcc structure in the ΓKLUX plane and its relation to the surface Brillouin zone for a [111]-oriented crystal. Free-electron final state model in an extended zone scheme for YH_2. The free-electron final state spheres (V_0=13 eV, ϕ=3.1 eV) are drawn for the Fermi energy and a binding energy of −3 eV. Shown in thick black is the Fermi surface contour, which was obtained via calculating the eigenstates on a cubic *k* space grid, which is shown with open circles. The occupied region is shown hatched for one pocket. Features one, two and three denote regions of coincidence between the free-electron final state of E_F and the Fermi surface contour. Feature four shows a possible Fermi surface nesting vector (see text). Contributions of a second domain are shown in gray. (c) Fermi surface and bulk BZ.

If one varies the photoelectron detection angle θ, one follows the corresponding FEFS sphere and automatically samples different states along the FEFS sphere in the BZ. One notices in Fig. 2(b) that a scan in the SBZ corresponds only superficially to a high-symmetry direction in the bulk BZ. The discrete nature of the photon energy restricts the *k* space sampling to a certain region in *k* space. The exact *k* space location is determined by the radius of the FEFS sphere and the dimensions of the BZ of the material. The FEFS sphere is determined via equation one and extends beyond the first BZ, hence we work in an extended zone scheme. Inscribed are FEFS spheres for initial states at the Fermi level and for a binding energy of −3 eV. Regarding the remaining parameters, we use reasonable values for the work function and the inner potential of ϕ=3.1 eV and V_0 =13 eV, respectively. Shown in black (gray for the mirror domain) is furthermore a calculated Fermi surface contour, which is based on a grid in *k* space, where the grid points are shown as open circles.

If one measures the energy distribution of photoelectrons, which are emitted normal to the surface, one samples a region in *k* space between Γ and *L*. Figure 2(b) shows that the FEFS is found between Γ and *L*. For increasing emission angles, various other high-symmetry lines are crossed. Special emphasis is drawn to the Γ *K X* and Γ *L* line in the extended zone scheme, which will be later employed to compare experimental data and theoretical data along high symmetry lines in more detail. If one compares the FEFS sphere and the corresponding constant energy surface for a specific binding energy one expects high photoemission intensities if the two coincide. Specifically for e.g., the Fermi energy, this would be the case around the points one and two [Fig. 2(b)], where the final state sphere cuts through the Fermi surface contour and around region three, where the Fermi surface is for a large *k* point range in the immediate vicinity of the FEFS sphere.

Figure 2(c) shows a three-dimensional representation of states at the Fermi level, based on the same potential that was utilized to generate the Fermi energy contour in Fig. 2(b). A three-dimensional contour plot[34] in *k* space of states at the Fermi energy correspondingly yields the three-dimensional Fermi surface. Clearly visible are the open necks along the Γ*L* direction. The discussed Fermi surface is a hole surface, which means that the occupied states are concentrated around the *X* point and not around the Γ point, as it is common for the free-electron metals. The occupied region is hatched for one pocket in Fig. 2(b) and correspondingly in Fig. 2(c) the occupied regions are found between the calculated Fermi surface and the various Brillouin zone boundaries.

Experimentally these Fermi surface contours can be probed via measuring the angular dependence of the photoemission intensity originating from states at the Fermi level. In Fig. 3 we present so-called Fermi surface maps for the studied dihydrides, which were obtained at room temperature. The intensity of He I excited photoelectrons, with energy centered at E_F, was mapped via Eq. (2) to $k_\parallel$. The outer circle corresponds to a polar angle of 90°, and the center of the image represents normal emission. Intensities are linearly color coded, high intensities (in white) result at $k_\parallel$ locations,

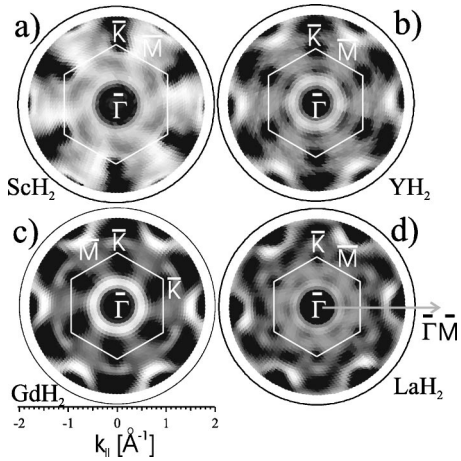

FIG. 3. Fermi surface maps measured with He I radiation, high intensities are shown in white, outer ring corresponds to 90° emission, center corresponds to normal emission, all intensities are shown in parallel projection, the raw data are symmetrized and divided by a background of Gaussian shape; the high-symmetry points and the SBZ are indicated. The size difference of the SBZ originates from the different lattice constants. (a) ScH_2, (b) YH_2, (c) GdH_2 and (d) LaH_2.

where direct transitions move through E_F. The mapping corresponds to a section through the Fermi surface perpendicular to the [111] direction, as has been demonstrated for the example of Cu (Ref. 23) and sketched for YH_2 in Fig. 2(b). All Fermi surface maps show a six-fold symmetry. The apparent doubling of symmetry compared to the trigonal [111] axis is due to the existence of the aforementioned two domains, which are rotated 180° with respect to each other.

The most prominent feature of the presented Fermi surface maps is an almost circular feature centered around the $\bar{\Gamma}$ point, in the middle of each image. The exact dimensions of this feature vary slightly. In general one observes a Fermi surface crossing, displayed as region of high intensity between 11° and 14°. This corresponds via Eq. (2) from 0.4 to 0.5 $Å^{-1}$. A very similar feature is sampled in the second surface BZ as well, noticeable as half circles in the outer parts of the map. One observes it only partially due to the limited k range via excitation with He I radiation. Moreover a clear drop in intensity at the $\bar{K}$ point can be recognized. Besides this, one notices a general high background intensity, especially in k space between the ringlike central part and the boundaries of the SBZ with additional slight intensity variations. The underlying band dispersion, which leads to the intensity enhancement at the Fermi level is investigated via complementary high-resolution scans along high-symmetry directions of the SBZ. For this purpose we recorded 31 photoelectron spectra in a range between 0° and 60° along the $\bar{\Gamma}$ $\bar{M}$ direction (as indicated by an arrow in Fig. 3(d). For this direction we measured the photoelectron intensity not only at the Fermi level but for binding energies between 0.2 and −7.48 eV. The data sets were mapped onto a regular $(E_i, k_\parallel)$ grid. In Fig. 4 the second derivative of the corresponding momentum distribution curves are visualized as gray scale plots with white corresponding to maximum intensity. The

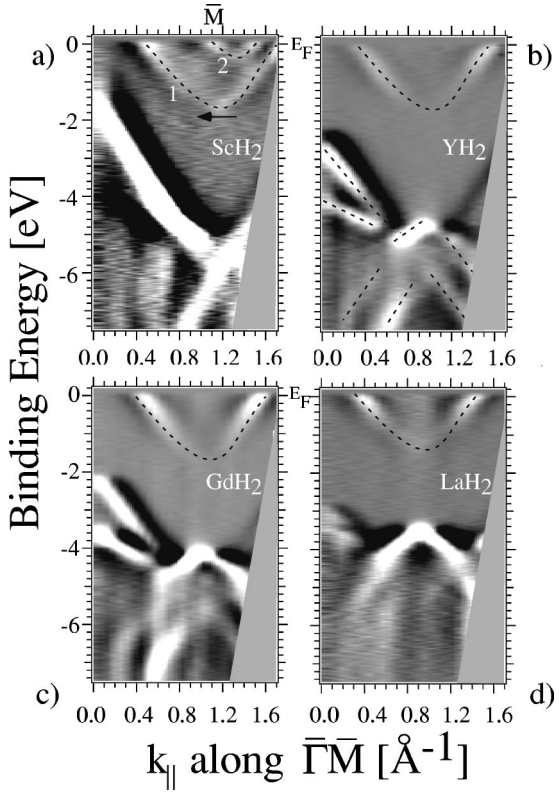

FIG. 4. Second derivative of experimental momentum distribution curves (a) ScH_2, (b) YH_2, (c) GdH_2 (d) LaH_2, color coded such that white corresponds to high intensity, the dashed lines serve as guide to the eye.

reason for taking the second derivative is a contrast enhancement (typical spectra are displayed in Fig. 6 below).

The obtained $E(k)$ plots (Fig. 4) are complementary to the measured Fermi surfaces in terms of being able to analyze more thoroughly the origin of enhanced intensity at the Fermi level. For the $\bar{\Gamma}$ $\bar{M}$ direction we can therefore assign a band to the observed circular feature in the Fermi surface maps. This band cuts the Fermi level at ≈0.4 $Å^{-1}$ and then disperses towards higher binding energies with increasing parallel wave-vector component. It exhibits a clear minimum at the SBZ boundary, at the $\bar{M}$ point. The band and its minimum is marked in Fig. 4(a) as feature 1. We find a binding energy of ≈ −1.6 eV at the extremal point. The k-space location of this minimum is different for the different compounds, since the different lattice constants manifest themselves in different SBZ dimensions, $k=2\pi/a$, ranging from 1.31 $Å^{-1}$ to 1.11 $Å^{-1}$. This effect becomes apparent in the Fermi surface maps, as a zoom-out impression, when comparing ScH_2 and LaH_2. Correspondingly one notices in the electron distribution curves a horizontal shift of the band minimum to lower $k_\parallel$ values [indicated in Fig. 4(a) with an arrow]. Furthermore one notices for ScH_2 and LaH_2 additional regions of high intensity close to the Fermi level in the inside of the aforementioned band, close to the $\bar{M}$ point. This feature is labeled as 2 for ScH_2. These additional intensities are different for the investigated compounds. For ScH_2 an almost empty electron pocket becomes visible in the electron

distribution curves (marked as feature 2). A very similar feature appears (though markedly weaker) for LaH_2 as well.

In order to facilitate a more in-depth comparison between experimental and theoretical results, one has to consider the measurement geometry and the FEFS model in conjunction with the theoretical band structure. For the states at the Fermi level one can immediately interconnect the FEFS sphere and its relation to the computed Fermi surface contour. For states with higher binding energy one can eventually compute the theoretical dispersion relation within this FEFS model for a comparison to experimental $E(k)$ curves.

We concentrate on YH_2 for the calculations but stress the applicability to ScH_2, GdH_2, and LaH_2. Following the discussion in Sec. III A, one notices that only one band (exception ScH_2, where the calculation yields a small contribution from band 2, see Fig. 1(a) contributes to the Fermi surface. Direct transitions are now expected for k points, where the FEFS sphere coincides with the Fermi surface in the extended zone scheme, as shown in Fig. 2(b).

The corresponding circle cuts the Fermi surface contour at the points labeled as 1 to 3. Initial states of k space region one [Fig. 2(b)] yield the primary circular feature around the $\bar{\Gamma}$ point. The crossing between FEFS circle and Fermi surface contour at point 2 in Fig. 2(b) yields the semicircle in the second SBZ. Furthermore the FEFS sphere coincides with the Fermi surface around region three. These points simultaneously appear for the $\bar{\Gamma}\bar{M}$ and the $\bar{\Gamma}\bar{M}'$ directions due to the existence of two mirror domains. Hence one observes in between point one and two an additional increase of photoemission intensity due to initial states at point three. It has to be pointed out, that in this region the choice of the FEFS parameters are quite crucial, since the sphere and the contour barely touch each other. This peculiar topology is responsible for the additional intensity around the $\bar{M}$ point. Since the FEFS does not cut but merely touches the initial state contour, one expects not sharp transition but more a diffuse background for this region, as it is indeed observed experimentally (Fig. 3). With regard to the slight deviations in between the investigated dihydrides, we have to assume that they stem primarily from effects due to the measurement geometry and due to the free electron final state assumption and are not signs of principal differences of the band structure in this energy region.

Via the FEFS model one can plot the eigenvalues of the appropriate k points for a measurement in $\bar{\Gamma}\bar{M}$ direction and obtain computationally a conventional $E(k)$ relation. The corresponding computed energy distribution curves [Fig. 5(b)] correspond very nicely in the energy range between 0.2 and −2 eV to the measured curves of Fig. 5(a). The topology of the sampled band is nicely reproduced. At the $\bar{M}$ high symmetry point of the SBZ, states in the environment of the X point of the bulk BZ are sampled. This particularly holds true for states at E_F, while for states at E_B=−3 eV k points in the vicinity of L and K are sampled (compare to Fig. 2(b)). Our combined measurements (Fig. 4) clearly indicate that the observed d-band width is constant for the measured dihydrides. This finding is theoretically very well reproduced. We find a binding energy of −1.6 eV, which is in excellent agreement

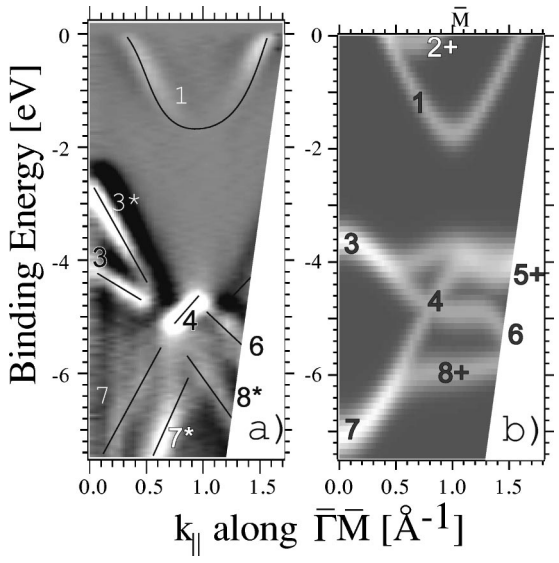

FIG. 5. Experimental and theoretical $E(k)$ for YH_2. (a) Second derivative of experimental $E(k)$ distribution curves (b) theoretical $E(k)$ distribution, eigenvalues were computed on a k grid, which is adapted to the experimental $E(k)$ distribution curves, both inequivalent domains (see text) are considered.

to the position of band 1 at the X point in Fig. 1.

With regard to the sampling of this band, we notice the appearance of a second feature [labeled as 2+ in Fig. 5(b)] which is due to the existence of a second mirror domain (especially for ScH_2 and LaH_2), we notice the appearance of a second feature [labeled as 2+ in Fig. 5(b)]. The exact location in energy and momentum is very dependant on the parameters of the FEFS and therefore leaves ample room to maintain the picture of an isoelectronic Fermi surface for the dihydrides, despite slight differences in the measurements.

In terms of testing the LDA band structure we have not discussed so far the hydrogen related bands, which are not in such close proximity to the Fermi level. The band-structure calculations predict two additional bands at higher binding energies, which have been labeled band 2 and band 3 in Fig. 1. The application of the FEFS model places these bands at −3.6 eV and 7.2 eV for normal emission [bands 3 and 7 in Fig. 5(b)]. Subsequently if one follows the dispersion along the $[\bar{\Gamma}\bar{M}]$ direction, the two bands split up in up to four bands, an effect which again is due to the existence of the aforementioned mirror domain. With regard to the comparison between measurement and theoretical results, we note for this energy range between −2 eV and −7.48 eV a less convincing agreement.

In order to stress the similarities between the different materials, we present in Fig. 6(a) electron distribution curves in the vicinity of the $\bar{M}$ point for ScH_2, YH_2, GdH_2, and LaH_2. These spectra were measured at 30° emission angle along the $[\bar{\Gamma}\bar{M}]$ direction, which translates via Eq. (2) to 1.08 Å^{-1} and is in the vicinity of the d-band minimum [feature 1 in Fig. 4]. The presented spectra in Fig. 6(a) are therefore part of the already presented energy distribution curves in Fig. 4, differing just in the data representation, which is now scaled to the true photoemission intensity and not to the

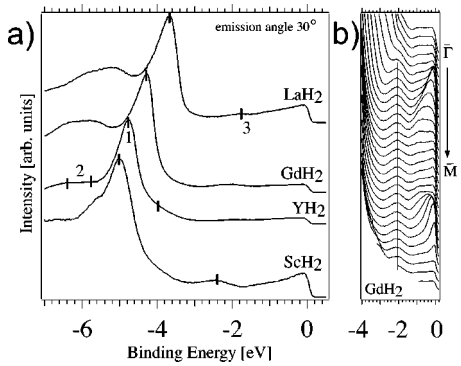

FIG. 6. (a) Experimental spectra ScH_2, YH_2, GdH_2 and LaH_2, all measured at an emission angle of 30°. (b) ARPES spectra along the $[\overline{\Gamma M}]$ direction for GdH_2 up to an emission angle of 60°.

second derivative, as it was the case in Fig. 4 and Fig. 5(a).

One notices again a very similar appearance for all measured dihydrides. The spectra are dominated by a peak at ≈ -3.7 eV for LaH_2 and -5 eV for ScH_2 [marked as feature 1 in Fig. 6(a)], which is below the previously discussed *d*-band minimum (feature 1 in Fig. 4). Even further below in energy additional structures (feature 2 in Fig. 6) can be distinguished. Emission from these H induced states is very strong. Compared to Fig. 4, now due to the intensity scale, almost no structure is found in the region between the Fermi level and -2 eV. As the only feature a small peak is visible at -1.8 eV (LaH_2) and -2.4 eV (ScH_2) and marked as feature three in Fig. 6(a). An inspection of the data set shows that a region of high intensity persists for all dihydrides in this energy range between -1.8 eV and -2.4 eV, and there is virtually no dispersion with the parallel wave-vector component. This absence of dispersion is highlighted in Fig. 6(b), where angle-resolved photoemission spectra along the $[\overline{\Gamma M}]$-direction for GdH_2 are shown. The feature does not show up in the plots of Fig. 4 because the derivative of the corresponding momentum distribution curves vanishes for nondispersing peaks. Such a nondispersive behavior is clearly inconsistent with the computed bandstructure, namely bands 1 to 3 in Fig. 1 and we tentatively assign this feature to structural imperfections, such as hydrogen in octahedral sublattice and/or tetrahedral vacancies.

We would like to point out that the *k*-space location around the $\overline{M}$ point represents a best case agreement to the computed band structure. For other *k* points (as shown in Fig. 4 and 5) one observes various discrepancies, whose origin might be speculated upon.

We try to classify theoretical and experimental bands into three groups; bands which are reproduced in theory and experiment (e.g., metal *d* bands) and bands which appear only in theoretical calculations or measurements. The two latter categories are denoted with a plus [theoretical bands 5+ and 8+ in Fig. 5(b)] and a star [experimental bands 3*, 7*, 8* in Fig. 5(b)].

The experimental observation of additional features (experimental bands 3*, 7*, 8*), which cannot be identified in theoretical bulk calculations might have a variety of possible reasons. The calculations were performed for the bulk structure and hence surface localized states are not included in the theoretical results. However we have no indication that these additional states are particularly sensitive to the formation of adsorbate layers as it would be typical for surface states. On the other hand the calculations assume a stoichiometric hydrogen concentration. However the absence of hydrogen vacancies and hydrogen impurities is experimentally difficult to ensure. The structural deviations in the hydrogen lattice would certainly affect the hydrogen induced states much more than the previously discussed metal *d* states. On the other hand a deviation to the calculated band structure might be a fingerprint of many-body physics, which has already been proposed in the context of the occurring Me-I transition (see Sec. IV). It seems that the occurence of additional states is a general feature for the dihydride phase since the splitting between feature 3 and feature 3* can be found not only for YH_2 but for GdH_2 and less clearly for LaH_2 as well (Fig. 4). The same holds true for feature 7* for YH_2 and GdH_2 and less clearly for LaH_2. ScH_2 seems to be exceptional in this sense, since it only exhibits one of the respective features.

In addition we note the absence of calculated bands in the experiment as it is the case for bands (5+ and 8+). The observation of eigenvalues in an experimental spectrum depends on the photoemission cross section for the specific transition. The corresponding matrix elements cannot at present be included in the calculation and might hamper the observation of these states. On the other hand, again a serious disorder in the hydrogen sublattice might as well be responsible for the disappearance of theoretically predicted bands in the experiment (Fig. 5).

In summary, one has to note that the comparison between the LDA calculations and the photoemission results is only very satisfactory in terms of band position and band topology for the metal derived *d* states. A one-to-one correspondence between calculation and experiment cannot be established for the H-derived states at higher binding energy.

IV. DISCUSSION

Apparently LDA is quite capable of describing the Fermi surface of rare-earth dihydrides, as can be judged from the agreement to the presented measurements. In view of the fact, that the pure elements do not have identical Fermi surfaces, it is especially intriguing that the hydrogenation of these different elements seems to yield a universal dihydride Fermi surface. Without discussing in detail the electronic structure of pure Sc,Y, Gd, and La, it has to be considered that the following different properties are generally ascribed to deviating Fermi surfaces. The doubling of the unit cell for La (e.g., its dhcp structure) has been already attributed to a Peierls-type distortion initiated by the removal of a nested part of the Fermi surface.[35] The occurrence of antiferromagnetic ordering for Gd-Y (Ref. 36) alloys and the occurrence of ferromagnetic order for pure Gd has been explained by differences in the nesting properties of the Fermi surface of Y and Gd. Apparently the structural transition between the pure metal and the dihydride removes these differences and yields a universal Fermi surface. It would be certainly highly beneficial to extend these photoemission studies to over- and

under-stoichiometric dihydrides, in order to monitor *in situ* the establishment and existence range of this universal *precursor* state for the rare earth hydrides.

In accordance to Gupta[37] for ErH_2 we find experimentally and computationally for all considered dihydrides a multiply connected hole surface, that is comprised of a distorted cube with necks protruding along the Γ L-directions. It is well known that large parallel sections of a Fermi surface are prone to be annihilated by the formation of a charge/spin-density wave.[38] Intuition would point for this Fermi surface to a nesting vector, which connects opposite sides of the cube and hence a nesting vector in [001]-direction (label 4 in Fig. 2(b)). Gupta and Burger[32] quantified this nesting vector with approximately $[0.4,0,0]\times 4\pi/a$ for ErH_2. It was pointed out by Liu,[39] that the corresponding ordering phenomena for such a nesting vector have so far not been observed in experiments.[40] Liu[39] proposed an alternative nesting vector $[\psi,\psi,1-\psi]$, where ψ is a materials dependant parameter. The ordering wave vector arises by considering an extended zone scheme and apparently complies more with the experimental results. In order to discuss this issue we have integrated the obtained band structure to obtain the generalized susceptibility $\chi(\mathbf{E},\mathbf{k})$, which quantifies the linear electronic response to a perturbation with wave vector $\mathbf{q}$ according to Eq. (3),[41]

$$\chi(E,\mathbf{q}) = \int \delta(\epsilon_{\mathbf{k}+q} - \epsilon_{\mathbf{k}})d\mathbf{k}. \qquad (3)$$

In this expression ϵ is the eigenvalue for a given wave vector $\mathbf{k}$ and $\mathbf{q}$ is the spanning vector between nested parts of the Fermi surface. The band index is omitted since only one band contributes to the Fermi surface. Figure 7(a) displays the susceptibility for inital states in the vicinity of E_F (integration over a small window $E=100$ meV) in the [100] plane of YH_2 shown in a grayscale representation, where black corresponds to large values of χ. The calculations were performed for spanning vectors $\mathbf{q}$ between $\mathbf{q}=(0,0)$ and (1,1) (in units of the conventional reciprocal lattice vector $4\pi/a$). A sketch of the Fermi surface contours in the ΓXWK plane is shown as an inset. Figure 7(b) shows a cut along the x-axis $(q,0)$ of the same susceptibility matrix.

We note regions of high susceptibility along the lines $(q,0)$ and $(0,q)$ with a maximum [marked with a circle in Fig. 7(a)] for a displacement vector, which corresponds to twice the Fermi wave vector and is close to the proposed value from Gupta.[32] Such a behavior would be consistent with a Peierls like scenario for various ordering phenomena.[38] We have to note however, that the wave-vector dependent part of the susceptibility does not exhibit strong fluctuations or a divergence in the calculated plane. The proposed nesting vector does not lead to a pronounced maxima in the susceptibility [Fig. 7(b)]. The diagonal contributions to the susceptibility from q vectors in [110] direction (marked as feature 1 in the inset) are comparable to the contributions in [100] direction. For the [100] direction we note a very high susceptibility for excitations with small q (feature 3 in inset) compared to the proposed nesting vector (feature 2 in inset). In this sense the Fermi surface is not heavily nested

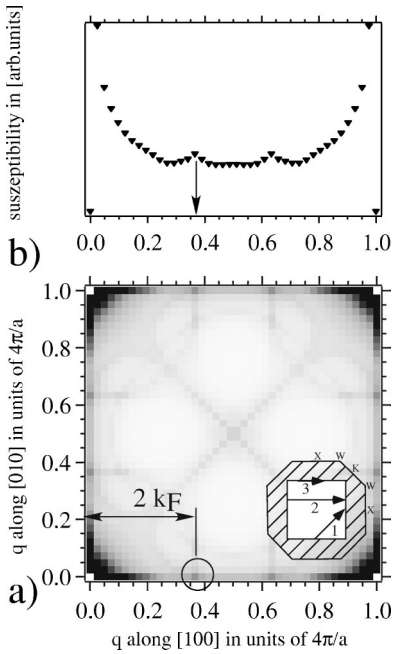

FIG. 7. (a) Susceptibility of YH_2 in the [100] plane, derived from LDA band structure; grayscale with dark regions corresponding to high susceptibilities. (b) Susceptibility in the [100] direction, yielding only small variations (indicated by arrow) due to weak Fermi surface nesting (see text).

along the principal axis of the warped cube. This fact might explain, why the search for parallel sheaths of the Fermi surface in order to explain experimentally observed nesting phenomena has not been successful so far.

Fermi surface nesting has been proposed for the trihydride phase as well[5] in conjunction with the complicated YH_3 atomic structure. It would be worthwhile to consider the electronic response to the addition of hydrogen atoms in vacant octahedral substitutional sites. First of all one might explain the ordering phenomena in superstoichiometric dihydrides[42] and secondly one might get more insight into the Me-I transition, which occurs at even higher hydrogen concentration, close to the trihydride phase.

With regard to the still ongoing debate on the origin of the insulating trihydride phase, one finds in the literature two different approaches.[43] One either argues on the basis of standard electron gas theory enriched by strong electron-phonon coupling (weak correlation approach) or one employs strong electron correlations to explain the large band gap of the trihydride phase. The weak correlation proposal certainly suffered from a still ongoing debate about the exact crystallographic structure of YH_3 and the absence of a broken symmetry structure in the twin compound LaH_3.

Van Gelderen[11,12] pointed out, that the failure of LDA can be traced back to an incomplete LDA description of the H ground state. This artifact directly stems from deficiency of the local exchange-correlation potential. Surprisingly the here presented data and calculations show a very nice agreement between LDA calculations and the dihydride phase for states in the immediate vicinity of the Fermi level. These bands originate from d-bands, centered at the metal sites. For binding energies below -2eV the agreement between experi-

ment and calculation is less convincing. From a phenomenological point of view it seems that the dihydride phase already exhibits traces of many-electron phenomena but yet still with an unperturbed Fermi surface. Only the addition of octahedral hydrogen leads to a collapse of this Fermi surface and correspondingly to the Me-I transition. Therefore it seems appropriate to pinpoint the failure of LDA to the description of hydrogen in general and in particular involving octahedral hydrogen. This in turn is related to the scenarios of Eder[8] and particularly Ng,[9] which assigned a crucial role to octahedral hydrogen. Judging from the observed isoelectronic nature of all dihydrides it is therefore very tempting to understand the dihydride phase as a *precursor* phase for the subsequent formation of the insulating trihydride phase.

V. CONCLUSIONS

We presented ARPES data on single crystalline [111]-oriented ScH_2, YH_2, GdH_2, and LaH_2 thin films on W(110). It was experimentally shown, that the Fermi surface is very similar for the studied compounds. Most prominent features of the Fermi surface are necks along the ΓL-direction, which originate from a band, which has a minimum at the $\bar{M}$ point at ≈ -1.6 eV binding energy in the ARPES experiments for all the investigated dihydrides. This state is very well reproduced via calculations based on a FEFS model. The observed universal Fermi surface for the measured dihydrides lets us propose that hydrogenation induces a common electronic precursor state, namely, a common Fermi surface, which is then annihilated for the subsequent hydrogen induced Me-I transition for the trihydride phase.

ACKNOWLEDGMENTS

We would like to acknowledge valuable discussions with D. Naumović, O. Gröning, and L. Schlapbach. We are greatly indebted to our workshop and electric engineering team, including O. Raetzo, E. Mooser, R. Schmid, R. Vonlanthen, Ch. Neururer, and F. Bourqui. Financial support by the Fonds National Suisse pour la Recherche Scientifique is gratefully acknowledged.

*Electronic address: Christian.Koitzsch@gmx.ch; URL: http://www.unine.ch/phys/

†Present address: SenTec AG, Ringstrasse 39, CH-4106 Therwil, Switzerland.

[1] P. Vajda, *Handbook on the Physics and Chemistry of Rare Earths* (Elsevier, Amsterdam, 1995), Vol. 20.

[2] J. Huiberts, R. Griessen, J. Rector, R. Wijngaarden, J. Dekker, D. de Groot, and N. Koeman, Nature (London) **380**, 231 (1996).

[3] T. Richardson, J. Slack, R. Armitage, R. Kostecki, B. Farangis, and M. Rubin, Appl. Phys. Lett. **78**, 3047 (2001).

[4] P. Kelley, J. Dekker, and R. Stumpf, Phys. Rev. Lett. **78**, 1315 (1997).

[5] Y. Wang and M. Chou, Phys. Rev. Lett. **71**, 1226 (1993).

[6] J. Hayoz, C. Koitzsch, M. Bovet, D. Naumovic, L. Schlapbach, and P. Aebi, Phys. Rev. Lett. **90**, 196804 (2003).

[7] A. van Gogh, E. Kooij, and R. Griessen, Phys. Rev. Lett. **83**, 4614 (1999).

[8] R. Eder, H. Penn, and G. Sawatzky, Phys. Rev. B **56**, 10 115 (1997).

[9] K. Ng, F. Zhang, V. Anisimov, and T. Rice, Phys. Rev. Lett. **78**, 1311 (1997).

[10] T. Miyake, F. Aryasetiawan, H. Kino, and K. Terakura, Phys. Rev. B **61**, 16 491 (2000).

[11] P. van Gelderen, P. A. Bobbert, P. Kelly, and G. Brocks, Phys. Rev. Lett. **85**, 2989 (2000).

[12] P. van Gelderen, P. A. Bobbert, P. Kelly, G. Brocks, and R. Tolboom, Phys. Rev. B **66**, 075104 (2002).

[13] P. Blaha, K. Schwarz, G. Madsen, D. Kvasnicka, and J. Luitz, (2001), *wien2k, An Augmented Plane* Wave+Local *Orbitals Program for Calculating Crystal Properties* (Karlheinz Schwarz, Tech. Univ. Wien, Austria).

[14] J. Perdew, S. Burke, and M. Ernzehof, Phys. Rev. Lett. **77**, 3865 (1996).

[15] J. Hayoz, T. Pillo, A. Zuettel, S. Guthrie, P. Aebi, and L. Schlapbach, J. Vac. Sci. Technol. A **18**, 2417 (2000).

[16] C. Koitzsch (unpublished).

[17] O. Rader and A. M. Shikin, Phys. Rev. B **64**, 201406(R) (2001).

[18] J. Osterwalder, T. Greber, A. Stuck, and L. Schlapbach, Phys. Rev. B **44**, 13 764 (1991).

[19] D. Naumović, A. Stuck, T. Greber, J. Osterwalder, and L. Schlapbach, Phys. Rev. B **47**, 7462 (1993).

[20] C. Fadley, *Synchrotron Radiation Research: Advances in Surface Science* (Plenum, New York, 1990), Vol. 1.

[21] J. Hayoz, S. Sarbach, T. Pillo, D. Naumovic, P. Aebi, and L. Schlapbach, Phys. Rev. B **58**, R4270 (1998).

[22] P. Aebi, J. Osterwalder, P. Schwaller, L. Schlapbach, M. Shimoda, T. Mochiku, and K. Kadowaki, Phys. Rev. Lett. **72**, 2757 (1994).

[23] P. Aebi, J. Osterwalder, R. Fasel, D. Naumovic, and L. Schlapbach, Surf. Sci. **307-309**, 917 (1994).

[24] T. Pillo, L. Patthey, E. Boschung, J. Hayoz, P. Aebi, and L. Schlapbach, J. Electron Spectrosc. Relat. Phenom. **97**, 243 (1998).

[25] Pearsson, *Pearsson's Handbook of Crystallographic Data for Intermetallic Phases* (American Society for Metals, Metals Park, OH, 1985).

[26] S. Gotennier, *Density Functional Theory and the Family of (L)APW Methods: a Step-by-Step Introduction*, available online at www.wien2k.at/reg_user/textbooks

[27] J. Weaver, D. Peterson, and R. Benbow, Phys. Rev. B **20**, 5301 (1979).

[28] J. Osterwalder, Z. Phys. B: Condens. Matter **61**, 113 (1985).

[29] L. Schlapbach, J. Osterwalder, and H. Siegmann, J. Less-Common Met. **88**, 291 (1982).

[30] A. Switendick, Int. J. Quantum Chem. **5**, 459 (1971).

[31] A. Switendick, Solid State Commun. **8**, 1463 (1970).

[32] M. Gupta and J. Burger, Phys. Rev. B **22**, 6074 (1980).

[33] D. Misemer and B. Harmon, Phys. Rev. B **26**, 5634 (1982).

[34] The three-dimensional contourplot was generated with MathGl3D, an extension to Mathematica from Wolfram Research, to be found at http://phong.informatik.uni-leipzig.de/kuska/mathgl3dv3/index.htm

[35] G. Fleming, S. Liu, and T. Loucks, Phys. Rev. Lett. **21**, 1524 (1968).

[36] H. Fretwell, S. Dugdale, M. Alam, D. Hedley, and A. Rodriguez-Gonzalez, Phys. Rev. Lett. **82**, 3867 (1999).

[37] M. Gupta, Solid State Commun. **27**, 1355 (1978).

[38] G. Gruner, *Density Waves in Solids* (Perseus, Boulder, CO, 2000).

[39] S. Liu, Solid State Commun. **61**, 89 (1987).

[40] R. Arons and J. Schweizer, J. Appl. Phys. **53**, 2645 (1982).

[41] I. Mazin and D. Singh, Phys. Rev. Lett. **82**, 4324 (1999).

[42] J. Shinar, B. Dehner, R. Barnes, and B. Beaudry, Phys. Rev. Lett. **64**, 563 (1990).

[43] A number of authors proposed the opening of a gap due to symmetry lowering via wavelike modulation of H atoms in the complicated HoD_3 structure. In view of an equivalent electronic structure of LaH_3 which apparently does not exhibit these wavelike modulations, a broken symmetry/charge density wave scenario has become rather doubtful.